Electronic supplementary information (ESI)

Bait-and-Anchor Strategy in Dual N/Se-Engineered Resins for Electrostatic-Chelation Cascade Pd(II) Recovery from Extreme Environments

Fan Wu, Hao Li,* Chuangen Zheng, Yanan Huang, Jianming Pan*

School of Chemistry and Chemical Engineering, Jiangsu University, Zhenjiang 212013, Jiangsu, China.

E-mail: haoli5385@ujs.edu.cn; pjm@ujs.edu.cn.

Contents

1. Materials and methods

1.1 Reagents and materials

Selenium powder (Se), sulfonyl chloride (SO_2Cl_2), phenol (C_6H_5OH), resorcinol ($C_6H_6O_2$) and palladium chloride ($PdCl_2$) were purchased from Aladdin (Shanghai, China). Chloroform ($CHCl_3$), thiourea (CH_4N_2S), Sodium carbonate (Na_2CO_3), anhydrous ether ($C_4H_{10}O$), ammonia ($NH_3 \cdot H_2O$), formaldehyde solution (CH_2O) and ethanol (EtOH), potassium chloride (KCl), sodium chloride (NaCl), ferric chloride ($FeCl_3$), calcium chloride ($CaCl_2$), zinc sulfate heptahydrate ($ZnSO_4 \cdot 7H_2O$), magnesium chloride ($MgCl_2$), copper (II) chloride dihydrate ($CuCl_2 \cdot 2H_2O$), nickel sulfate hexahydrate ($NiSO_4 \cdot 6H_2O$), N-hexane (C_6H_{14}), ethyl acetate ($C_4H_8O_2$) and hydrochloride (HCl) were purchased from Sinopharm (Shanghai, China). RTS-82 chelating resin was purchased from Rutian Environmental Protection Technology Co., Ltd (Hubei, China). All of the reagents above were used directly without further purification and deionized water was used for all experiments.

1.2 Characterization

The morphologies of the materials were analyzed using scanning electron microscopy (SEM, Quanta FEG 250, FEI, USA) and transmission electron microscopy (TEM, Hitachi-HT7800, Japan). Fourier-transform infrared (FTIR) spectra across the range of 4000 to 400 cm^{-1} were recorded using a Nicolet NEXUS-470 FTIR spectrometer (USA). The elemental composition, specifically carbon (C), hydrogen (H), and nitrogen (N), was determined by elemental analysis using a Flash 1112A analyzer (USA). Zeta potential measurements were conducted with a NanoBrook 90Plus PALS instrument. X-ray photoelectron spectroscopy (XPS) was performed on a Thermo Scientific K-Alpha instrument using Al Kα radiation (hν = 1486.6 eV), with binding energies referenced to the C1s peak at 284.8 eV. Palladium (II) ions and other ions were quantitatively analyzed through inductively coupled plasma optical emission spectrometry (ICP-OES, VISTA-MPX, Varian). In-situ infrared spectroscopy was carried out to monitor the growth and adsorption processes of the resins using a

Nicolet Is10 spectrometer in both drifts and attenuated total reflectance (ATR) modes. In-situ Raman spectroscopy was recorded using a inVIA/DM 2500M, Renishaw.

1.3 Density functional theory (DFT) calculations

All the DFT calculations were performed by the Gaussian 16 package [1]. Geometry optimization of all structures was performed using the M06-2X functional [2], with the TZVP basis set [3]. Frequency calculations were performed to obtain the Gibbs free energy correction. The Gibbs free energy of proton is obtained by summing up the Gibbs free energy correction with its hydration free energy (-262.4 kcal/mol) [4] and its concentration term -RTln(1E-7).

2. Experimental procedures

2.1 Preparation of Bis(4-hydroxyphenyl) Selenide (BHPS)

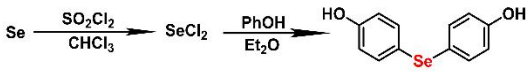

The monomer containing Se and phenol structures was synthesized following a previously reported protocol [5]. Initially, 1.58 g of Se powder was introduced into 40 mL of chloroform and dispersed under magnetic stirring. Subsequently, a mixture of 2.7 g of sulfonyl chloride and 40 mL of chloroform was incorporated and stirred until achieving homogeneity. Following this, 3.76 g of phenol, in combination with 40 mL of anhydrous ether, was introduced and stirred until the solution achieved clarity and transparency. The reaction proceeded at room temperature for 3 h before a 21 wt% Na_2CO_3 solution was gradually added dropwise until no gas evolution was observed. The resulting organic phase was separated using a separatory funnel, and the organic solvent was evaporated using rotary evaporation. The obtained product underwent further purification via column chromatography, ultimately yielding a final product in the form of a golden solid. **^{1}H NMR (400 MHz, d$_6$-DMSO, Fig. S4) δ (ppm):** 10.00 (s, 1H, -OH), 7.54-7.44 (m, 2H, Ar-H), 7.20-7.10 (m, 2H, Ar-H), 2.50 (s, 1H, DMSO-d6).

2.2 Preparation of N-doped RF resin microspheres (RF)

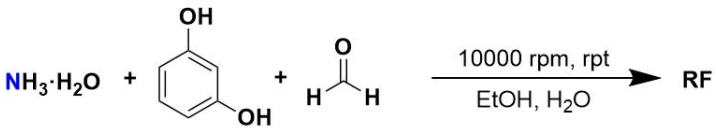

In general, 70 μL of ammonia (28 wt%) was added to a certain proportion of ethanol-water solution and 70 mg of resorcinol was dispersed using ultrasound. Then 70 μL of formaldehyde water solution was added and then stirred at 10000 rpm for 5 min at room temperature. The resultant solid was separated by centrifugation, washed multiple times with water and ethanol, yielding RF, which was then thoroughly dried under vacuum conditions.

2.3 Preparation of Se, N-doped RF resin microspheres (Se-RF)

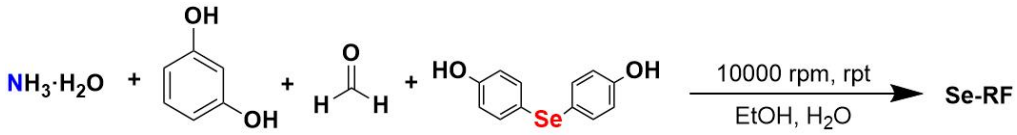

Typically, a predetermined volume of ethanol-water solution was prepared, to which 70 μL of ammonia (28 wt%) was added. Sequentially, 10 mg of resorcinol and 25 mg of BHPS were dispersed ultrasonically in the solution. Following this, a 70 μL solution of formaldehyde in water was introduced, and the resulting mixture was stirred at 10000 rpm for 5 min at room temperature. Subsequently, the resulting solid was separated by centrifugation and washed several times with water and ethanol. The resulting product, Se-RF, was then thoroughly dried in a vacuum oven to obtain the final product.

2.4 Bath adsorption experiments

To investigate the adsorption performance of RF/Se-RF towards Pd(II), experiments were conducted to examine the effects of solution pH, adsorption kinetics, isotherms, and other relevant parameters. Additionally, the adsorption mechanism was proposed based on characterization analyses. Testing solutions were prepared by diluting a 1.0 M Pd(II) standard solution, with solution pH adjusted using either 1.0 M HCl or 1.0 M NaOH. Unless otherwise specified, for each adsorption experiment, 5.0 mL of the testing solution and 2.0 mg of sorbents were mixed. After adsorption, separate the solid adsorbent by centrifugation and take the supernatant for testing. The concentrations of Pd(II) and other ions before and after adsorption were determined using ICP-OES. The adsorption capacity at different time points (Q_t, mg g^{-1}) and the equilibrium adsorption capacity (Q_e, mg g^{-1}) were calculated using Eq. (S1) and Eq. (S2), respectively. All experiments were conducted in triplicate, and the results were averaged for analysis. The calculation equations of adsorption capacity at different times (Q_t, mg g^{-1}) and equilibrium adsorption capacity (Q_e, mg g^{-1}) [6]:

$$Q_t = \frac{(C_0 - C_t)V}{m} \quad \text{(S1)}$$

$$Q_e = \frac{(C_0 - C_e)V}{m} \quad \text{(S2)}$$

where C_0 (mg L^{-1}), C_e (mg L^{-1}) and C_t (mg L^{-1}) are the initial concentration, equilibrium concentration, and the concentration at *t* time of adsorbate, respectively. *V* (L) is the volume of the testing solution, and *m* (mg) is the weight of sorbent.

2.5 Experimental steps for regeneration

The regeneration of Se-RF was conducted through an adsorption-desorption cycle. After adsorption of Pd(II) at pH 2.0 for 2 h at room temperature, the used adsorbent was separated from the solution and transferred into a desorption solution containing 0.5 M thiourea and 0.1 M HCl. The mixture was stirred for 2 h at room temperature to desorb Pd(II). The Se-RF was then thoroughly washed several times with deionized water until the wash water reached a neutral pH, followed by drying at 60°C for 12 h. The regenerated Se-RF was subsequently reused in repeated adsorption cycles to evaluate its reusability and stability.

2.6 Preparation of actual samples

In order to prepare actual samples for testing, palladium containing waste catalysts generated during the chemical production process were selected. 2.0 g of waste catalyst is first treated with aqua regia to dissolve palladium and other metal components. After 48 h, filter the solution to remove insoluble residues, and then dilute to volume with deionized water. Adjust the pH of the obtained solution to 2.0 using 1M HCl or NaOH.

3. Experimental results and discussion

3.1 Optimization of preparation conditions

Ethanol, an organic solvent, significantly influences the morphology of the microspheres by modifying the dielectric constant and surface tension of the solution. A higher ethanol proportion effectively reduces the solution's surface tension, facilitating the formation of smaller and more uniform microspheres. Additionally, the rapid evaporation of ethanol is advantageous for the swift formation and solidification of microspheres during high-speed stirring. However, excessive ethanol can decrease the solution's viscosity, potentially compromising the structural integrity and mechanical strength of the microspheres. Concurrently, the ammonia solution acts as an alkaline catalyst [7], enhancing the polymerization kinetics by providing a favorable environment for the condensation reactions between resorcinol and formaldehyde. This catalytic action is crucial for achieving desired polymer network structures within the forming microspheres. Therefore, precise control over the ethanol-to-water ratio and the amount of ammonia, tailored to specific application requirements, is crucial for optimizing the synthesis of RF/Se-RF microspheres.

This work investigated the effects of alcohol/water ratio and the amounts of monomers and catalyst on the synthesis of Se-RF by systematically adjusting the preparation conditions. In order to ensure sufficient reaction and better investigate the role of each component, ultrasound assisted synthesis of Se-RF is adopted here. SEM analysis revealed significant morphological variations: In **Fig. S1a**, a solvent volume ratio of 2:5 (ethanol to water), supplemented with 35 μL of ammonia and an appropriate proportion of bis(4-hydroxyphenyl) selenide (BHPS) and resorcinol, yielded uniform and well-dispersed spherical microspheres with diameters of approximately 200 nm. These conditions provided a balanced solvent ratio and alkaline environment, ensuring sufficient monomer availability for uniform polymerization, thus forming microspheres with high polymerization degree and larger particle size. In contrast, **Fig. S1b** shows that reducing the ammonia volume, while maintaining other conditions constant, led to significant microsphere aggregation and branching. This suggests that an insufficient alkaline environment

hindered uniform polymerization, resulting in uneven reaction kinetics and poorly controlled microsphere formation. **Fig. S1c** further illustrates that a decrease in monomer dosage, coupled with an increased ammonia volume, exacerbated the dispersion issues, leading to larger aggregates and irregular structures. This outcome indicates that higher ammonia levels accelerate the reaction rate, but reduced monomer levels lead to fewer nucleation sites, promoting in situ growth and irregular microsphere formation. Finally, **Fig. S1d**, with an adjusted ethanol to water ratio of 1:6, displayed higher uniformity and smaller microsphere sizes, with an average diameter of about 150 nm. This adjustment suggests that increased water content can moderate the reaction kinetics, allowing for finer control over polymerization and resulting in smaller, more uniform microspheres.

In summary, the ethanol-to-water ratio, the quantity of monomers and the ammonia decisively influence the morphology and size of the phenolic resin microspheres. Optimizing these parameters allows for precise control over microsphere morphology. The appropriate formulation not only ensures desired morphological traits but also enhances the microspheres' practical performance, such as adsorption efficiency and chemical stability. Therefore, considering the minimum particle size and appropriate dispersibility, the material ratio in **Fig. S1d** was chosen as the ideal ratio for subsequent experiments.

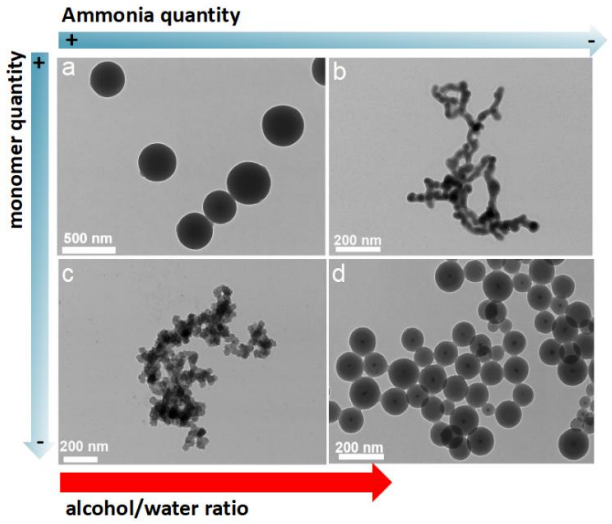

Figure. S1 SEM images of RF under different preparation conditions.

3.2 Particle size management

RF resin, a crucial sorbent, has broad applications in environmental remediation and industrial processes [8]. The efficiency and stability of adsorption in RF-based resins are highly dependent on particle size, underscoring the importance of effective particle size control. Traditional approaches to regulating particle size have been unwieldy by complexity and inefficiency, necessitating the development of more streamlined and efficacious techniques. This work presents a novel method that utilizes high-speed stirring to regulate particle size, distinguishing itself with its simplicity and effectiveness, and avoiding the use of complex chemical methods to achieve particle size management.

This section elucidates the analysis of SEM images and particle size distribution graphs of RF prepared at varying stirring speeds: untreated, 5000 rpm, 10000 rpm, and 15000 rpm (**Fig. S2**). By comparing the untreated sample to those subjected to incremental stirring speeds, we assess the influence of high-speed stirring on the particle size and distribution of RF. The control sample (untreated) exhibits a broad particle size distribution, as indicated by a flat curve, reflecting significant size heterogeneity. Although the shapes of the particles are similar, their sizes vary noticeably. At 5000 rpm, the particle size distribution curve becomes narrower, peaking at a smaller size, which suggests enhanced uniformity and reduced particle size compared to the untreated sample. SEM images reveal particles with more consistent and regular morphology. With treatment at 10000 rpm, the particles demonstrate further uniformity, as shown by an even tighter particle size distribution curve with a sharper peak at a smaller size. SEM images show a highly uniform assembly of particles with minimal size variation. At the highest stirring speed of 15000 rpm, the SEM images shows some small particles, which is consistant with the distribution curve peaks. The trend observed suggests that appropriate stirring speeds result in more uniform particle sizes. The mechanical energy imparted by stirring likely disrupts the aggregation of larger particle clusters and prevents the agglomeration of smaller ones, leading to a more uniform size distribution. With the further increase of stirring speed, the increase of particle size distribution indicates

that the nucleation and growth process of particles are greatly enhanced, leading to the formation of more small particles, which may be due to the rapid dispersion of reactants and intermediates, thus inhibiting the formation of large particles. These results corroborate the hypothesis that high-speed stirring is an effective method for controlling the particle size of RF, which is vital for their use in adsorption processes where surface area and porosity are key parameters. The precise control of particle size achievable through high-speed stirring suggests that this method could be extensively applied in the production of RF-based resins for various industrial applications, potentially enhancing their efficiency and homogeneity.

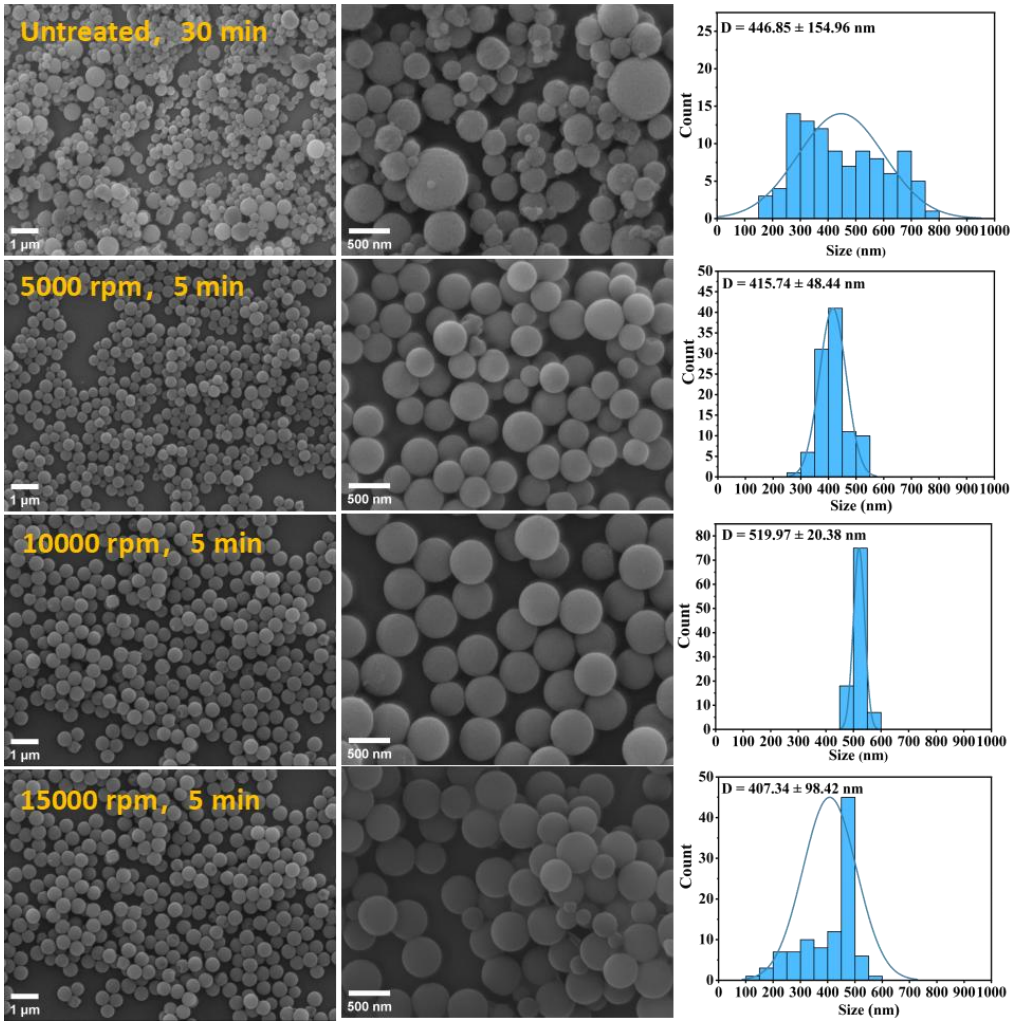

Figure. S2 SEM images of RF in the different preparation conditions (untreated for 30 min and 5000, 10000, 15000 rpm for 5 min).

3.3 The structural features of BHPS monomer

As shown in **Fig. S3-S4**, the XPS and ^{1}H NMR spectrum of BHPS monomer confirm the successful synthesis of BHPS.

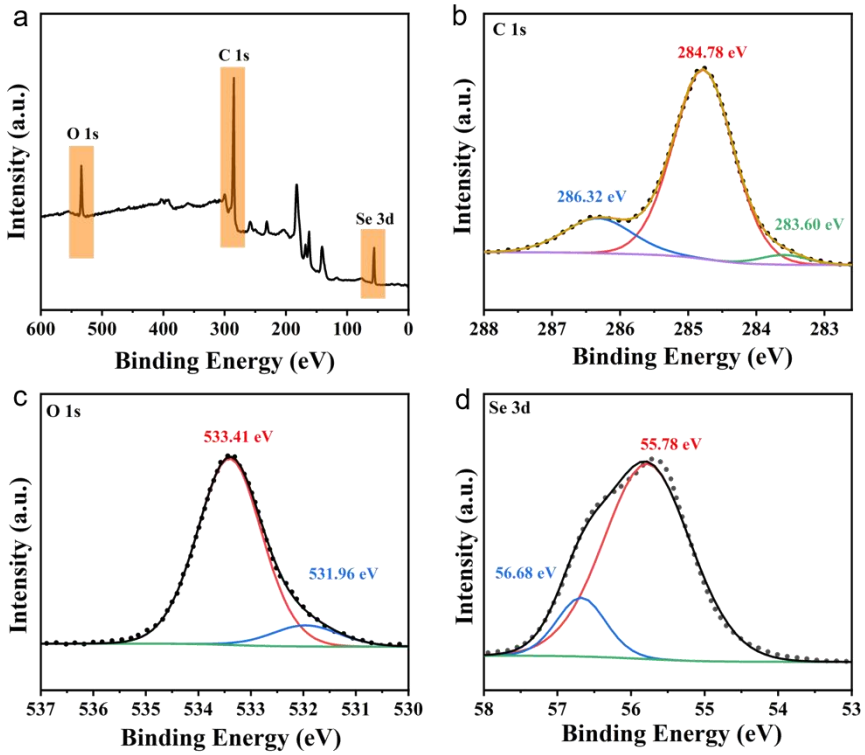

Figure S3. (a) The XPS spectra of BHPS monomer; (b) C 1s, (c) O 1s and (d) Se 3d high resolution XPS spectra of BHPS.

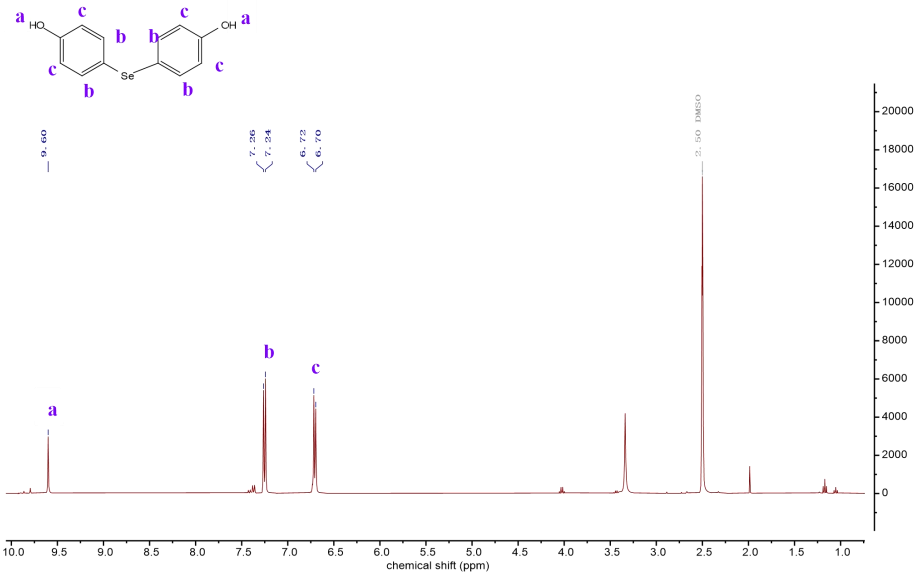

Figure. S4 ^{1}H NMR spectrum of BHPS (400 MHz, deuterated DMSO).

As depicted in **Fig. S5**, BHPS exhibits more complex absorption bands compared to resorcinol, particularly around 1000 cm^{-1}, due to the introduction of selenium and its more complex molecular structure. Additional peaks at 500-600 cm^{-1} correspond to Se-C bonds, while strong absorption at ~3400 cm^{-1} indicates OH stretching vibrations similar to resorcinol.

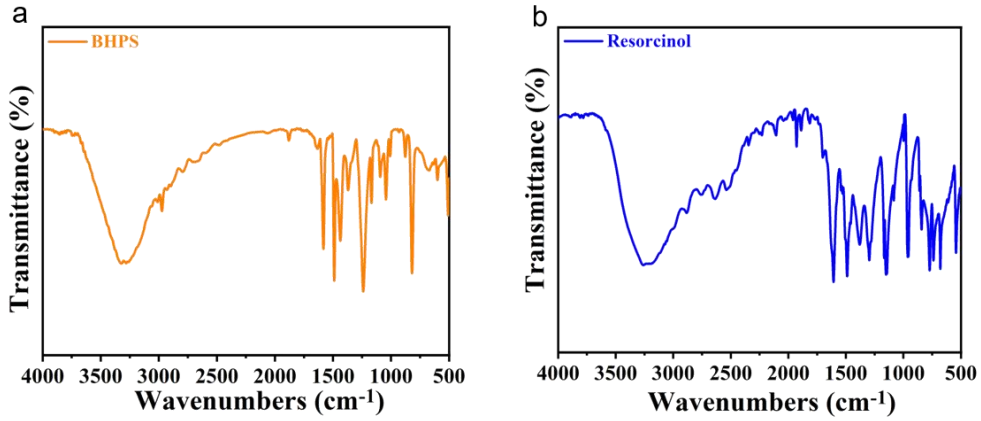

Figure. S5 FTIR spectrum of (a) BHPS monomer and (b) resorcinol.

Table S1 presents the BET surface area, pore structure, and elemental composition of RF and Se-RF. Selenium doping significantly enhances the specific surface area (25.41 $m^2\ g^{-1}$ vs. 18.82 $m^2\ g^{-1}$), pore volume (0.0972 $cm^3\ g^{-1}$ vs. 0.0575 $cm^3\ g^{-1}$), and average pore size (15.31 nm vs. 12.22 nm) of the resin. Elemental analysis shows a decrease in nitrogen content and an increase in carbon content in Se-RF, indicating structural and chemical modifications induced by selenium doping, which contribute to its improved adsorption performance.

Table S1. BET and elemental analysis data of RF and Se-RF.

Sorbent	BET			Element analysis			
	Specific Surface Area ($m^2\ g^{-1}$)	Pore Volume ($cm^3\ g^{-1}$)	Pore Size (nm)	N (wt%)	C (wt%)	H (wt%)	S (wt%)
RF	18.82	0.0575	12.2216	8.94	56.14	5.83	0
Se-RF	25.41	0.0972	15.3061	4.99	58.85	5.41	0

Contact angle measurements (**Fig. S6**) further demonstrate that both RF and Se-RF are highly hydrophilic, with contact angles below 20°.

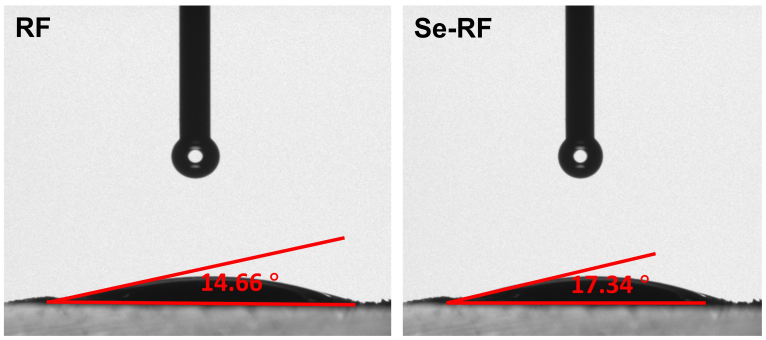

Figure. S6 Contact angle data of RF and Se-RF.

3.4 Investigation of N-doped RF growth mechanism

Density functional theory (DFT) calculations were used to study the changes of Gibbs free energy in the resin formation path with and without N, so as to reveal the possible mechanism of resin formation. **Table S2** lists the energies of some transition states in the reaction process.

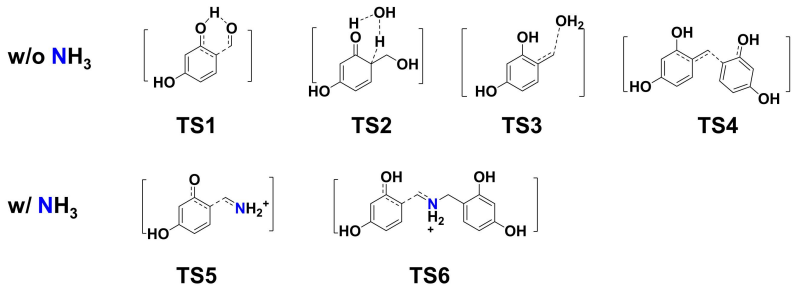

Table S2. Free energy data table of chemical reaction related substances with/without ammonia conditions

	G (a.u.)	G (kcal/mol)		G (a.u.)	G (kcal/mol)
phenol	-382.611299				
NH_3	-56.530802				
H_2O	-76.419435				
HCHO	-114.491710		HCHNH	-94.602259	0.5
TS1	-497.060221	26.8	$HCHNH_2$	-95.040985	3.4
1	-497.089582	8.4	TS5	-477.625882	20.0
TS2	-573.487325	22.0	7	-477.626025	19.9
2	-497.116338	-8.4	8	-477.228658	-9.0
H^+	-0.443371		9	-515.304412	-11.1
3	-497.520698	16.1	10	-515.742733	-8.0
TS3	-497.509307	23.3	TS6	-898.322544	11.8
4	-421.095607	19.7	11	-898.323558	11.1
TS4	-803.696931	25.9	12	-897.923246	-15.9
5	-803.716327	13.8			
6	-803.314393	-12.2			

3.5 pH effect of adsorption

The adsorption performance of RF and Se-RF for Pd(II) strongly depends on pH, as it affects the surface charge of the adsorbent and the speciation of Pd(II). Pd ions exist in various forms under different pH conditions, such as $PdCl_3^-$, $PdCl_4^{2-}$, $PdCl^+$ and so on (**Fig. S7**) [9]. It can be seen that negatively charged $PdCl_4^{2-}$ and $PdCl_3^-$ are dominant when pH ≤ 3, which influence their interaction with the adsorbent. As illustrated in **Fig. 4a**, Se-RF consistently demonstrates higher adsorption capacities across the pH range of 1–4 compared to RF. Specifically, the adsorption capacity of Se-RF increases initially and reaches its maximum at pH 2, and then declines slightly as the pH rises to 3 and 4. This trend suggests that selenium doping enhances Pd(II) adsorption by introducing additional active sites or improving surface interactions. In contrast, RF shows a pronounced decrease in adsorption capacity at pH 4. This reduction maybe attributed to the diminished protonation of nitrogen-containing groups, leading to weaker electrostatic interactions with Pd(II). Conversely, Se-RF maintains relatively stable adsorption at higher pH levels, indicating that selenium enhances non-electrostatic interactions with Pd(II), such as complexation.

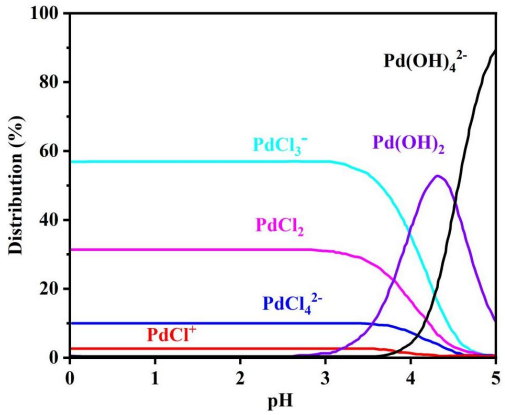

Figure. S7 Distributions of the Pd(II) complexes ([Pd_{tot}] = 0.001 M) estimated at [Cl_{tot}] = 0.01 M as a function of pH.

As shown in **Fig. 4b**, the Zeta potential of RF decreases to its lowest value at pH 1 and then increases sharply, peaking at pH 2 before decreasing again as the pH rises further. This trend reflects significant changes in surface charge, likely due to the ionization of hydroxyl groups and their interactions with Pd(II). In contrast, Se-RF

shows a steady and linear increase in Zeta potential across the pH range, indicating that selenium doping stabilizes the surface charge, reducing charge fluctuations. The behavior of Se-RF suggests that selenium doping enhances the electronic environment of the material's surface, allowing for consistent and efficient adsorption in weakly acidic conditions. This stabilization facilitates the formation of stable Se-Pd complexes, further improving the material's Pd(II) adsorption performance compared to RF. These results highlight pH 2.0 as the optimal condition for Pd(II) adsorption (**Fig. 4a**), where RF achieves its maximum Zeta potential, and Se-RF demonstrates stable and favorable surface interactions. The superior performance of Se-RF underscores the importance of selenium doping in enhancing adsorption efficiency and stability in weakly acidic environments. Based on these results, pH 2.0 was identified as the optimal condition for further adsorption studies.

3.6 Adsorption kinetics

The kinetic data were fitted with pseudo-first-order model (Eq. S3) and pseudo-second-order model (Eq. S4) [10, 11].

$$Q_t = Q_{max}\left(1 - e^{-k_1 t}\right) \quad \text{(S3)}$$

$$Q_t = \frac{k_2 Q_{max}^2 t}{1 + k_2 Q_{max} t} \quad \text{(S4)}$$

Q_{max} (mg g^{-1}) stands for maximum adsorption capacity, Q_t (mg g^{-1}) is adsorption capacity at time t, k_1 (min^{-1}), k_2 (g mg^{-1} min^{-1}) are adsorption rate constant respectively.

And the relevant parameters are summarized in **Table S3**. For RF, the pseudo-first-order model yields an R^2 value of 0.856, while the pseudo-second-order model provides a much better fit with an R^2 value of 0.971 (**Fig. 4c**). Similarly, for Se-RF, the pseudo-first-order model poorly fits the data (R^2 = 0.259), whereas the pseudo-second-order model achieves a high R^2 value of 0.956. These results suggest that chemisorption is the dominant mechanism for Pd adsorption. The experimental equilibrium adsorption capacity ($Q_{e,\,exp}$) of Se-RF is 287.60 mg g^{-1}, nearly double that

of RF (148.78 mg g^{-1}). Additionally, the equilibrium adsorption capacity calculated using the pseudo-second-order model ($Q_{e,c}$) for Se-RF closely matches the experimental value (286.31 mg g^{-1}), confirming the accuracy of the kinetic model in describing the adsorption behavior.

Table S3. Kinetic model parameters in Pd(II) adsorption of RF/Se-RF (C_0 = 100 mg L^{-1}).

Sorbent	$Q_{e,exp}$[a] (mg g^{-1})	Pseudo-first-order			Pseudo-second-order		
		k_1 (min^{-1})	$Q_{e,c}$[b] (mg g^{-1})	R^2	k_2 (g mg^{-1} min^{-1})	$Q_{e,c}$[c] (mg g^{-1})	R^2
RF	148.78	0.108	140.09	0.856	0.0010	149.89	0.971
Se-RF	287.60	0.634	282.90	0.259	0.0124	286.31	0.956

[a] $Q_{e,exp}$ is the experimental equilibrium adsorption amount, [b] $Q_{e,c}$ is the calculated equilibrium adsorption amount from the pseudo-first-order kinetic model, [c] $Q_{e,c}$ is the calculated equilibrium adsorption amount from the pseudo-second-order kinetic model.

3.7 Intraparticle diffusion model fitting

To further study the adsorption mechanism of Se-RF. in, the data were also fitted through the intra-particle diffusion model (S5), which can be divided into three steps: (I) surface diffusion, (II) intra particle diffusion process and (III) dynamic process of adsorption and equilibrium [10, 11].

$$Q_t = k_3 t^{0.5} + C \quad \text{(S5)}$$

Q_t (mg g^{-1}) is adsorption capacity at time t, k_3 (mg $g^{-1}\cdot min^{-1/2}$) is adsorption rate constant respectively. C represents the characteristic constant of the boundary layer.

As described in **Fig. S10**, the rapid initial adsorption seen in Se-RF within the first 15 minutes (named as the first stage), which is an external diffusion stage that Pd(II) is distributed on adsorption sites of the adsorbent surface, although intraparticle diffusion may influence the early stages of adsorption, it is not the rate-limiting step for Se-RF. In the second stage (20-60 min), the adsorption rate decreases with the decrease of adsorption sites. In the third stage (120-360 min), it could be viewed as a

process of simultaneous adsorption and desorption and reaching dynamic equilibrium. The parameters in **Table S4** show k_3 in the order $k_{3,I} > k_{3,II} > k_{3,III}$ and the intercepts of the three stages are $C_I < C_{II} < C_{III}$, indicating that surface adsorption is the control step. In summary, Se-RF demonstrates superior adsorption performance, faster intraparticle diffusion, and better kinetic fitting by the pseudo-second-order model compared to RF, further confirming the positive effect of Se in enhancing adsorption properties.

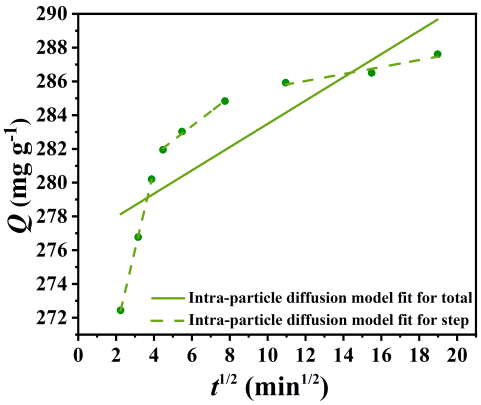

Figure. S8 Intra-particle diffusion model fitting data of Se-RF.

Table S4. The fitting parameters of the intra-particle diffusion model for Se-RF.

Se-RF	R^2	k_3 (mg g^{-1} min$^{-1/2}$)	C
Total	0.667	0.689	276.595
Stage I	0.999	4.739	261.825
Stage II	0.994	0.864	278.172
Stage III	0.939	0.206	283.545

3.8 Adsorption isotherms

Analyzing the adsorption isotherm data is essential for optimizing the preparation and application of adsorbents. Pd(II) adsorption experiments were conducted at varying temperatures (298 K, 308 K, and 318 K) and initial concentrations ranging from 50 to 500 mg L^{-1}, as shown in **Fig. S11**. To further investigate the nature and mechanism of adsorption behavior, the data were fitted using Langmuir and Freundlich isotherm models (Eq. S6-S7) [10, 11].

$$Q_e = \frac{Q_{max} k_L C_e}{1 + k_L C_e} \quad \text{(S6)}$$

$$Q_e = k_F C_e^{1/n} \quad \text{(S7)}$$

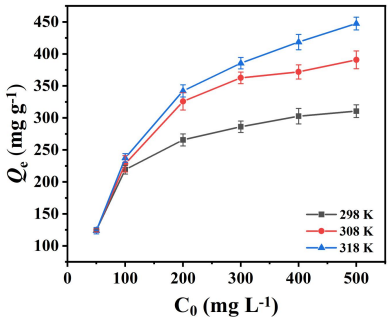

Figure. S9 The curve between C_0 and Q_e

The corresponding calculated parameters are listed in **Table S5**. The Freundlich isotherm model provided a better fit to the data, with R^2 values closer to 1 (0.995, 0.994 and 0.987), and the maximum Pd(II) adsorption capacity was 447.35 mg g^{-1}, superior to the Langmuir isotherm model, which had lower R^2 values (0.808, 0.726, and 0.884). Therefore, compared to the Langmuir isotherm model, the Freundlich isotherm model more accurately described the adsorption behavior of Pd(II) on Se-RF, indicating that the adsorption of Pd on Se-RF is a multilayer adsorption on a heterogeneous surface, suggesting that the adsorption mechanism is likely diverse.

Table S5. Adsorption isotherm constants in Pd(II) adsorption of Se-RF.

T (K)	Langmuir isotherm model			Freundlich isotherm model		
	Q_{max} (mg g^{-1})	K_L (L mg^{-1})	R^2	K_F (L$^{1/n}$·mg$^{(1-1/n)}$·g^{-1})	$1/n$	R^2
298	278.89	3.780	0.808	157.11	0.116	0.995
308	376.25	0.186	0.726	172.44	0.142	0.994
318	404.12	0.382	0.884	162.93	0.175	0.987

3.9 Adsorption thermodynamics

Thermodynamic parameters such as enthalpy change (ΔH, kJ mol^{-1}), entropy change (ΔS, J mol^{-1} K^{-1}) and Gibbs free energy change (ΔG, kJ mol^{-1}) can further provide other essential information about the adsorption mechanism and they are calculated using the equations (Eq. S8-S10) [12].

$$K_D = \frac{(C_0 - C_e)V}{C_e m} \quad \text{(S8)}$$

$$lnK_{\mathrm{D}} = \frac{\Delta S}{R} - \frac{\Delta H}{RT} \quad \text{(S9)}$$

$$\Delta G = - RTlnK_D \quad \text{(S10)}$$

Here K_{D} is the distribution coefficient, and R is the universal gas constant (8.314 $J{\cdot}K^{-1}{\cdot}mol^{-1}$).

Table S6 compares Se-RF in this work with some other resin-based adsorbents for Pd(II) adsorption in terms of adsorption capacity, adsorption equilibrium time and optimal pH [13-20]. It can be seen that Se-RF exhibits extremely high adsorption capacity and excellent adsorption kinetics for Pd(II).

Table S6. Comparison of Se-RF with other reported adsorbents.

Sorbents	Maximum adsorption capacity (mg g^{-1})	Equilibration time (min)	pH	References
Woven wool resin	19.50	1440	1.0	13
MBI/XAD7HP	126.20	480	0.3	14
MBT/XAD7HP	137.60	480	0.3	14
MBO/XAD7HP	98.40	720	0.3	14
PPF resin	259.70	1440	1.0	15
PGNR	114.30	60	4.0	16
CDCR	204.34	150	3.0	17
CysR	143.47	1080	2.0	18
SIR-1	52.77	150	0	19
MMBT/XAD7HP	137.60	540	0	20
Se-RF	447.35	60	2.0	This work
RTS-82	16.08	120	2.0	-

3.10 Selective adsorption

The selectivity of adsorbents has become a critical parameter to evaluate their performance. In fact, Pd inevitably coexists with various metal cations in the natural environment or waste, which greatly increases the difficulty of separating and recovering Pd. Additionally, during the acid hydrolysis of electronic waste, most other metal cations are simultaneously leached out. In this work, a simulated leaching solution with same concentration and acidity were were selected and configured into

to investigate the selective adsorption performance of RF/Se-RF. First, the corresponding amount of metal salt ($PdCl_2$, $FeCl_2{\cdot}4H_2O$, KCl, $CaCl_2$, $ZnSO_4{\cdot}7H_2O$, $MgNO_3{\cdot}6H_2O$, $CuCl_2{\cdot}2H_2O$ NaCl and $NiSO_4{\cdot}6H_2O$) was calculated and weighed. Notably, the concentration setting of 50 mg L^{-1} is significantly higher than that of the actual leaching solution (as will be mentioned in subsequent experiments), thereby amplifying the interference effect and more effectively reflecting the selective adsorption performance of RF and Se-RF. Dilute hydrochloric acid was added to dissolve and the pH was adjusted to 2.0 by HCl and NaOH. Then continue to use dilute hydrochloric acid solution with pH 2 to dilute to the required volume in a volumetric flask. The distribution coefficient (K_D), the selective coefficient (α) and the concentration coefficient (CF) calculated by Eq. (S8), Eq. (S11) and Eq. (S12) were used to evaluate the selective adsorption behavior of RF/Se-RF [12].

$$\alpha = \frac{K_D(\mathrm{Pd})}{K_D(\text{coexisting ions})} \tag{S11}$$

$$CF = \frac{Q_e}{C_0} \tag{S12}$$

The relevant parameters of the simulated leachate and the selective adsorption parameters are listed in **Table S7** and **Table S8**. As can be seen in **Fig. S10,** the Q_e, K_D and CF values of RF/Se-RF for Pd(II) are significantly higher than those of other coexisting cations, indicating the superior selectivity of these materials towards Pd(II). However, compared with Se-RF, RF has a larger adsorption capacity for the interfering ions and has a poorer selectivity. This may be attributed to the presence of N elements and a large number of phenolic hydroxyl groups in RF. According to hard-soft acid-base (HSAB) theory, Pd(II) is "soft acid", while heteroatoms (N and Se) are "soft base", there is a high affinity between them. It is obvious that Pd(II) is the softest cation among metal ions and has the highest $\Delta_f G$ value. These results indicate that the doping of Se enhances the adsorption selectivity of RF resin for Pd(II), allowing it to effectively separate and enrich Pd(II) in complex metal ion environments, thus demonstrating its potential in practical applications.

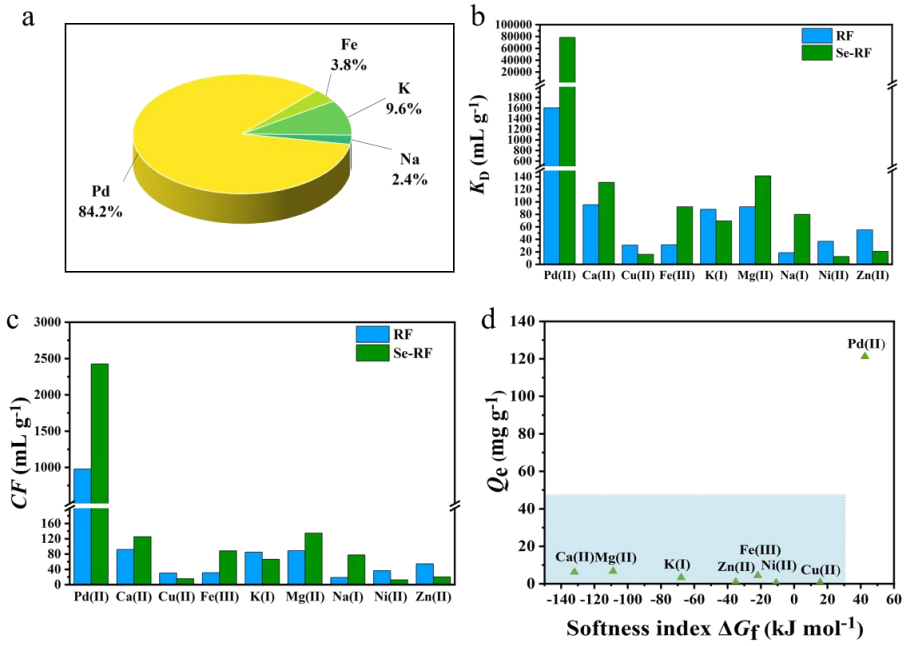

Figure. S10 (a) Metal components in the desorption solution of Se-RF; Selective adsorption data of RF/Se-RF: (b) distribution coefficient, (c) concentration factor towards of RF/Se-RF, (d) cation correlation "softness" index with Q_e values.

Tble S7. Components of simulated leachate and parameters of selective adsorption of RF

Metal ions	C_0 (mg L^{-1})	Q_e (mg g^{-1})	K_D (mL g^{-1})	α	CF (mL g^{-1})	Adsorption efficiency (%)	$\Delta_f G_M^{2+}$ (kJ moL^{-1})
Pd(II)	50.00	48.86	1604.52	1.00	977.29	39.09	42.49
Ca(II)	50.00	4.59	95.34	0.02	91.84	3.67	-132.12
Cu(II)	50.00	1.52	30.74	0.05	30.36	1.21	15.55
Fe(II)	50.00	1.55	31.34	0.05	30.95	1.24	-21.87
K(I)	50.00	4.25	87.90	0.02	84.91	3.40	-
Mg(II)	50.00	4.45	92.20	0.02	88.92	3.56	-108.83
Na(I)	50.00	0.93	18.66	0.09	18.52	0.74	-
Ni(II)	50.00	1.82	36.86	0.04	36.33	1.45	-10.90
Zn(II)	50.00	2.71	55.34	0.03	54.14	2.17	-35.17

Table S8. Components of simulated leachate and parameters of selective adsorption of Se-RF

Metal ions	C_0 (mg L^{-1})	Q_e (mg g^{-1})	K_D (mL g^{-1})	α	CF (mL g^{-1})	Adsorption efficiency (%)	$\Delta_f G_M^{2+}$ (kJ moL^{-1})
Pd(II)	50.00	121.28	78429.41	1.00	2425.50	96.91	42.49
Ca(II)	50.00	6.26	131.08	598.34	125.25	4.45	−132.12
Cu(II)	50.00	0.78	15.97	4911.29	15.50	2.94	15.55

Fe(II)	50.00	4.41	92.05	852.00	88.25	4.13	−21.87
K(I)	50.00	3.31	69.62	1126.52	66.25	4.84	-
Mg(II)	50.00	6.73	141.62	553.79	134.50	5.03	−108.83
Na(I)	50.00	3.89	79.98	980.66	77.75	2.78	-
Ni(II)	50.00	0.61	12.56	6244.59	12.25	2.46	−10.90
Zn(II)	50.00	1.01	20.84	3763.34	20.25	2.83	−35.17

3.11 Evaluation of Se-RF adsorption performance in practical applications

For practical applications, efficient and selective recovery of Pd(II) under harsh and complex conditions is highly desirable. In this work, a waste palladium-containing catalyst (**Fig. S11**), widely used in the chemical production industry, was selected as a representative practical sample. The recovery and reuse of such catalysts are of great significance for both environmental protection and resource conservation. The spent catalyst was first leached using aqua regia, and the pH of the resulting solution was adjusted to 2.0 after appropriate dilution, in accordance with common industrial practice prior to adsorption. The solution composition was analyzed, and the concentrations of major metal ions before and after adsorption are summarized in **Table S9**.

As shown by the adsorption results, Se-RF exhibits outstanding selective adsorption behavior toward precious metals in complex practical samples, particularly for Pd(II), demonstrating its strong potential for industrial application. To further elucidate the selective adsorption behavior of Se-RF toward different precious metal ions, static selective adsorption experiments were conducted using mixed Pd(II)/Au(III) solutions with different concentration ratios. As shown in **Fig. S12a**, at identical initial concentrations, the adsorption capacity of Se-RF for Au(III) is higher than that for Pd(II). This behavior can be attributed to the strong Lewis acid – base interaction between Au(III), a typical soft-acid metal ion, and selenium sites in Se-RF, leading to the formation of highly stable Au-Se coordination bonds. Even after adjusting the relative concentrations of Au(III) and Pd(II), Se-RF maintains a strong adsorption affinity toward Au(III).

Notably, when the concentration of Pd(II) in the system is significantly higher than that of Au(III) **(Fig. S12b-c**), the adsorption capacity of Se-RF for Pd(II) increases markedly. This concentration-dependent behavior can be explained by a synergistic adsorption mechanism. First, the interaction between Pd(II) and Se-RF involves not only Pd-Se coordination but also coordination and electrostatic interactions with nitrogen-containing sites, providing multiple adsorption pathways for Pd(II). Second, according to the law of mass action, a higher Pd(II) concentration increases the collision frequency between Pd species and adsorption sites, thereby dynamically enhancing the adsorption probability. In addition, the initial adsorption of Pd(II) may modulate the surface charge distribution or local coordination environment of Se-RF, creating more favorable conditions for subsequent Pd(II) uptake.

To further evaluate the selectivity of Se-RF in systems containing multiple platinum-group metals, competitive adsorption experiments between Pd(II) and Pt(IV) were performed under acidic conditions, and the results are shown in **Fig. S12d-f**. These results indicate that Pd(II) preferentially occupies the active sites of Se-RF, and the presence of Pt(IV) does not significantly suppress Pd adsorption. This selective behavior can be attributed to the cooperative "bait-and-anchor" mechanism: protonated nitrogen sites electrostatically pre-concentrate anionic palladium chloro-complexes, while selenium anchoring sites, acting as soft donor atoms, exhibit stronger coordination affinity toward soft-acid Pd(II) than toward kinetically inert Pt(IV) species.

To further validate the practical selectivity of Se-RF, RF (with N as the primary adsorption site), Se-RF (with dual N and Se sites), and a commercial thiourea-functionalized palladium extraction resin (RTS-82, containing N and S sites) were applied to the same batch of real leachate. As shown in Fig. S13, Se-RF demonstrates a significantly higher selective extraction capacity for Pd in complex systems compared with both RF and RTS-82, highlighting the critical role of selenium sites in enhancing Pd selectivity.

In summary, Se-RF exhibits strong and tunable selective adsorption behavior toward precious metal ions. Although Au(III) shows a higher intrinsic affinity under controlled conditions, Se-RF maintains excellent selectivity for Pd(II) in complex, Pd-rich practical systems, even in the presence of competing precious and base metal ions. This combination of high selectivity, robustness, and adaptability makes Se-RF particularly suitable for industrial-scale Pd recovery from secondary resources.

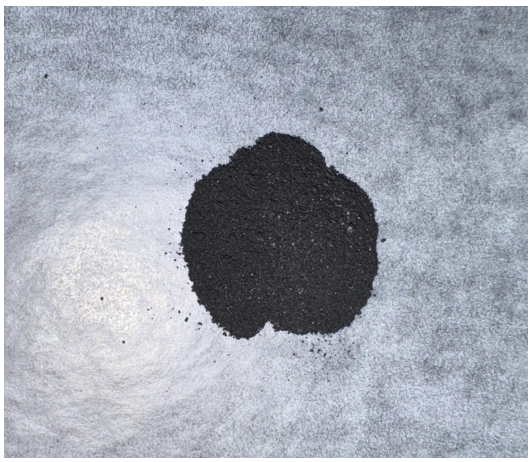

Figure. S11 Photo of waste catalyst (actual sample).

Table. S9 Detail data of actual sample recovery experiment using Se-RF.

Element	C^a (mg L^{-1})	C^b (mg L^{-1})	Adsorption ratio (%)
Fe	39.482	38.164	3.34
Ca	32.524	32.508	0.05
K	27.940	27.736	0.73
Al	15.860	15.725	0.85
Mn	5.839	5.836	0.05
Mg	5.551	5.474	1.39
Sr	2.032	1.998	1.69
Ti	1.150	1.023	11.09
Pd	0.598	0.020	96.65
Au	0.241	0.195	19.09
Zn	0.239	0.234	2.37
Y	0.189	0.186	1.97
Cr	0.135	0.132	2.08
Ni	0.103	0.102	0.57

[a]The concentration of the sample after acidification with aqua regia and dilution.

[b]The concentration of the sample after adsorption.

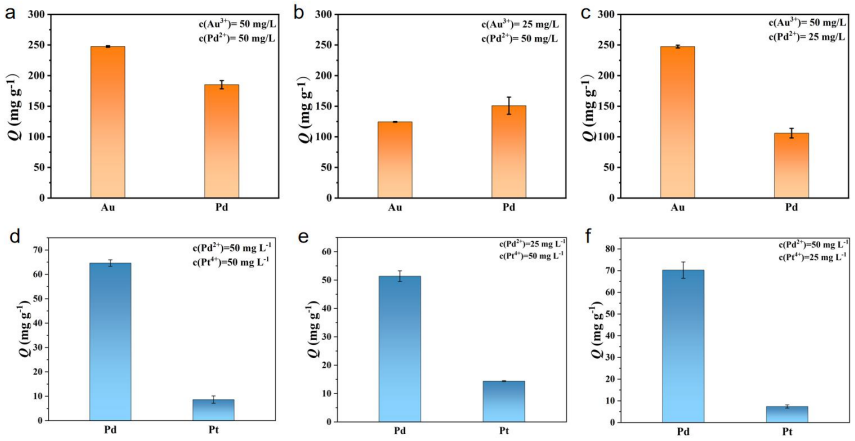

Figure. S12 Selective adsorption performance of Se-RF for Au(III)/Pd(II) and Pt(IV)/Pd(II) at different initial concentrations.

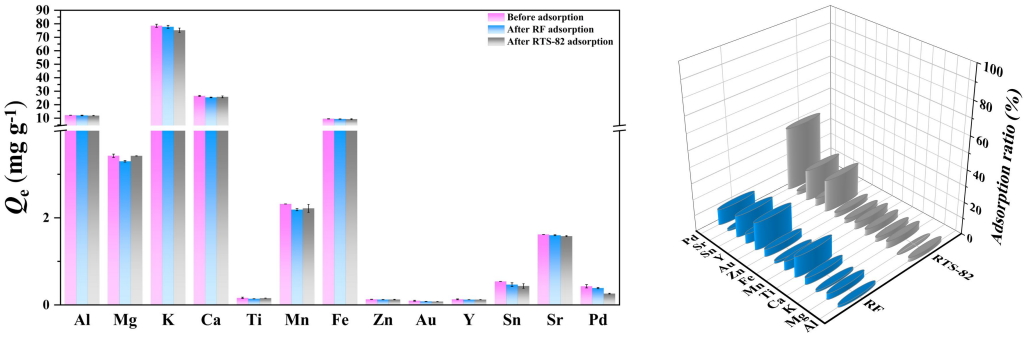

Figure. S13 Adsorption performance of RF/RTS-82 for actual sample.

3.12 Adsorption mechanism

The thermodynamic data for Pd adsorption on Se-RF at different temperatures are summarized in **Table S6**. **Fig. S14b** shows the Van't Hoff plot of lnK_D versus 1/T. The value of ΔG are -7.12 kJ mol^{-1}, -8.36 kJ mol^{-1} and -10.18 kJ mol^{-1} at 298 K, 308 K and 318 K, respectively, indicating that the adsorption process is spontaneous. The calculated ΔH value is 38.49 kJ mol^{-1}, indicating that the adsorption process is endothermic and that increasing temperature favors adsorption, consistent with the data in **Fig. S14a**. The value of the standard entropy change (ΔS) was 153.04 $J \cdot mol^{-1} \cdot K^{-1}$, reflecting a possible change in the adsorbent surface structure, increased randomness at the solid-liquid interface during the adsorption process, and redistribution of energy between the adsorbate and the adsorbent.

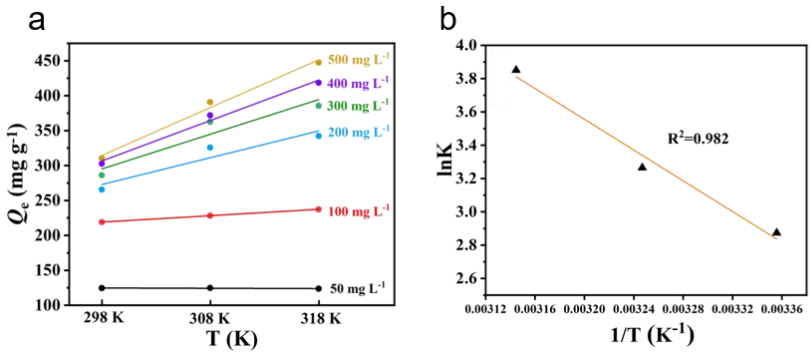

Figure. S14 (a) effect of temperature on the Pd(Ⅱ) adsorption by Se-RF; (b) Van't Hoff plot of lnK_D versus 1/T.

Table S10. Thermodynamic parameters obtained in adsorption of Pd(II) onto Se-RF.

T (K)	ΔG (kJ mol^{-1})	ΔH (kJ mol^{-1})	ΔS (J mol^{-1} K^{-1})
298	-7.12		
308	-8.36	38.49	153.04
318	-10.18		

After adsorption, the presence of Pd was confirmed by HRTEM energy-dispersive X-ray spectroscopy (EDS) elemental mapping (**Fig. S15**). The intrinsic elements of

Se-RF can be clearly found with this mapping, and the distribution of Pd elements indicates the successful adsorption of palladium.

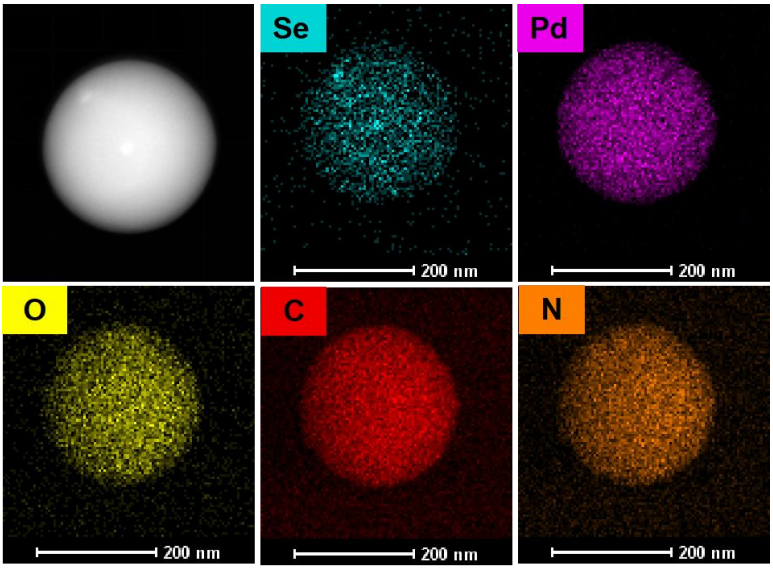

Figure. S15 HRTEM energy-dispersive X-ray spectroscopy (EDS) elemental mapping of Se-RF after palladium adsorption.

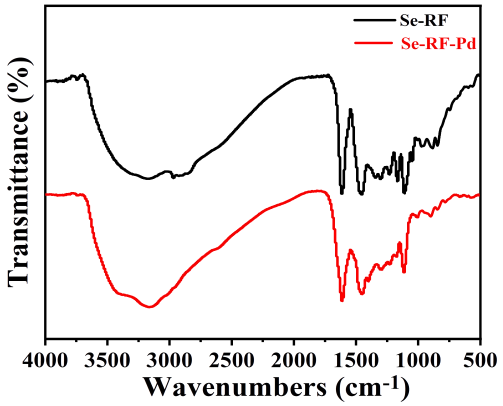

Figure. S16 FTIR spectra of Se-RF and Se-RF-Pd.

Fig. S17 and **Fig. S18** illustrate the *in situ* infrared and *in situ* Raman spectra of Se-RF and RF during the Pd(II) adsorption process. In **Fig. S18**, the FTIR spectra of Se-RF show significant changes over time, particularly in the regions corresponding to -OH stretching (~3400 cm^{-1}) and C-N/C-O stretching (~1200-1300 cm^{-1}). These changes indicate the active participation of hydroxyl and amine groups in Pd(II) binding through protonation and chelation. The evolution of peaks below 1000 cm^{-1}

reflects the formation of stable Se-Pd complexes, demonstrating selenium's role in enhancing adsorption performance. **Fig. S19a** presents the FTIR spectra of RF, showing similar functional group interactions during Pd(II) adsorption, but with less pronounced changes compared to Se-RF, highlighting the additional functionality provided by selenium doping. **Fig. S19b**, the Raman spectra, reveals characteristic peaks at ~800 cm^{-1}, which intensify over time and correspond to interactions between Pd(II) and active sites, primarily nitrogen in RF. The absence of significant shifts in other regions of the Raman spectra indicates that RF relies more on nitrogen-based interactions, whereas Se-RF benefits from a synergistic effect between nitrogen and selenium for improved adsorption efficiency.

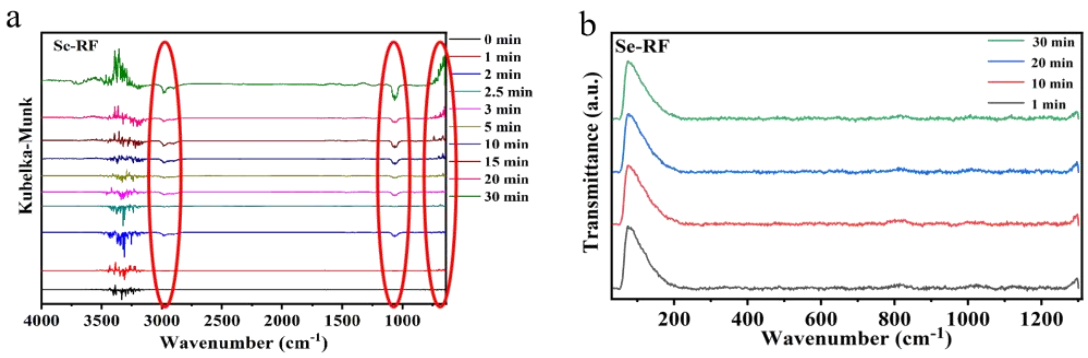

Figure. S17 *In situ* infrared spectra (a) and *in situ* Raman spectra of Se-RF during the Pd adsorption process .

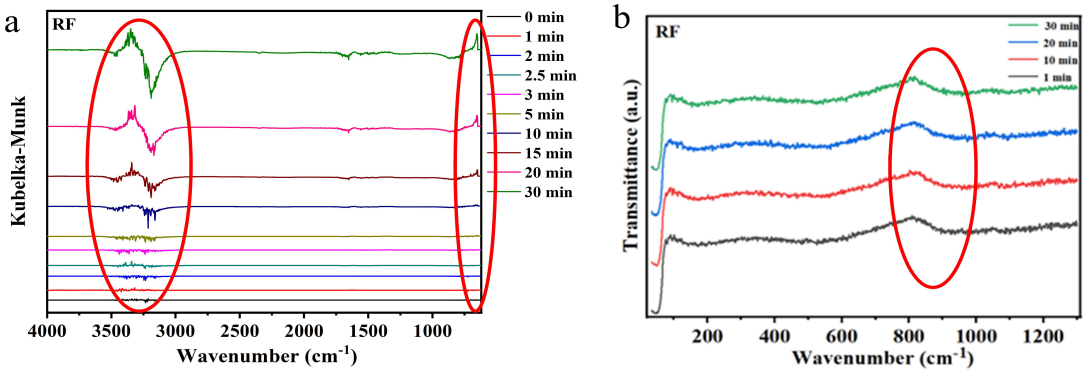

Figure. S18 I*n situ* infrared spectra (a) and *in situ* Raman spectra (b) of RF during the Pd adsorption process.

3.13 Further validation of the adsorption mechanism

The adsorption mechanism of Se-RF for Pd(II) was further validated by systematically adjusting the nitrogen and selenium content (Se-RF, Se-RF(1/2N), Se-RF(1/2Se)) in the material and examining their direct influence on Pd adsorption. The column chart (**Fig. S19**) highlights the substantial impact of N and Se content on the Pd adsorption capacity of Se-RF. Specifically, reducing the nitrogen or selenium content in Se-RF (as in the Se-RF (1/2 N) and Se-RF (1/2 Se) sample) led to a decrease in Pd adsorption capacity, highlighting the critical role of nitrogen in enhancing adsorption performance.

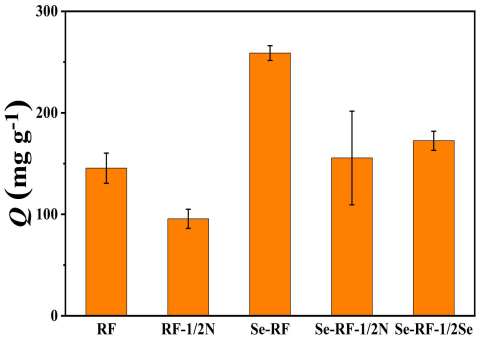

Figure. S19 The adsorption capacity of Pd(II) on samples prepared under different conditions.

3.14 DFT calculation data of the adsorption mechanism

DFT calculations revealed that N-doped sites exhibit strong electron-donating capabilities, forming the primary adsorption active center with the highest binding energy (-38.37 kcal/mol) for Pd^{2+}. In contrast, Se-doped sites alone showed weaker coordination, with a binding energy of only -19.14 kcal/mol. However, when Se cooperatively coordinates with N, the adsorption energy significantly improves to -28.35 kcal/mol, accompanied by a favorable Gibbs free energy change (ΔG = -22.07 kcal/mol), indicating enhanced thermodynamic stability. These results demonstrate that while Se is not the primary adsorption site, its participation enhances Pd^{2+} binding strength and adsorption selectivity through a synergistic coordination mechanism. The cooperative effect between N and Se provides multiple binding pathways and a sterically optimized structure, which is crucial for improving adsorption performance.

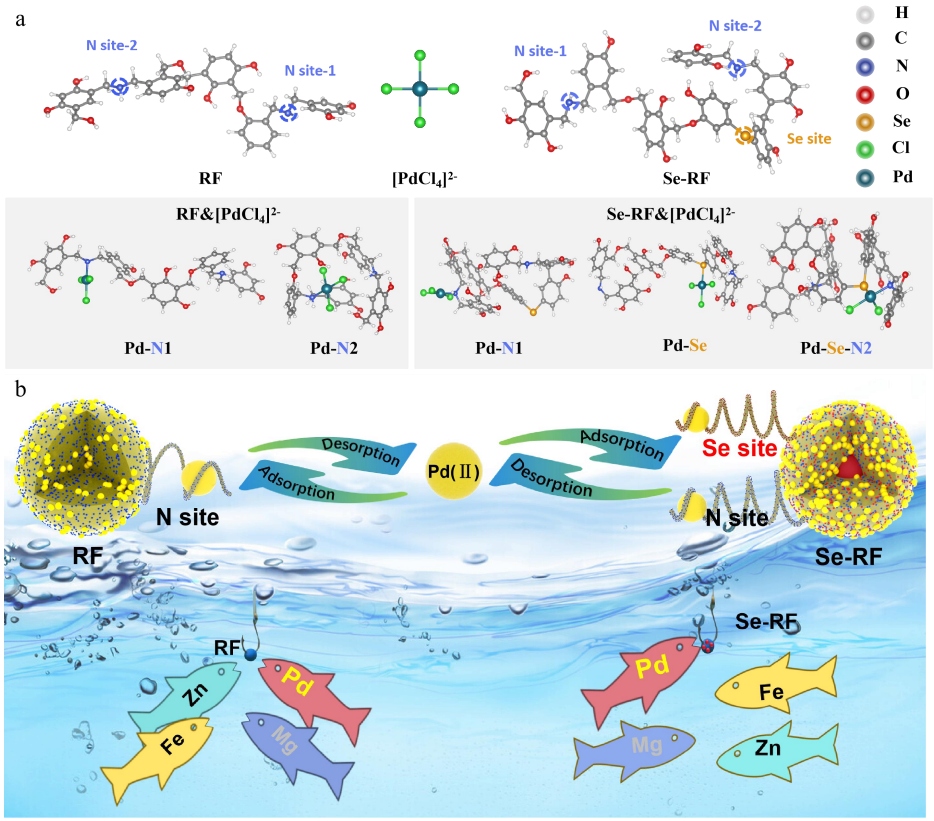

Figure. S20 (a) The optimized binding configuration of different coordination sites of RF/Se-RF with $[PdCl_4]^{2-}$; (b) Schematic diagram of enhanced adsorption of Pd(II) by Se-RF/RF.

.**Table. S11** Reaction energies (E) and binding energies (Eb) of Pd(II) interacting with various coordination sites in RF and Se-RF models, calculated by density functional theory (DFT).

	E (a.u.)	Eb (a.u.)	Eb（kcal/mol）
RF	-2331.99475		
Pd-N-1	-3840.42047	-0.061154	-38.37
Pd-N-2	-3840.39061	-0.031293	-19.64
Cl	-460.233752		
Pd	-1968.59832		
Se-RF	-5534.94037		
Pd-N-1	-7043.36166	-0.056733	-35.60
Pd-Se	-7043.33543	-0.030504	-24.72
Pd-Se-N	-6583.11636	-0.045181	-19.14

Table. S12 Thermochemical parameters, total Gibbs free energies (G), and changes in Gibbs free energy (ΔG) for Pd(II) coordination with different functional groups in RF and Se-RF systems.

	TCG	E (a.u.)	G (a.u.)	ΔG (a.u.)	ΔG (kcal/mol)
RF	0.644367	-2331.99475	-2331.350386		
Pd-N-1	0.656896	-3840.42047	-3839.763575	-0.0355	-22.28
Pd-N-2	0.64367	-3840.39061	-3839.74694	-0.018865	-11.84
Cl	-0.015023	-460.233752	-460.248775		
Pd	-0.028148	-1968.59832	-1968.626464		
Se-RF	0.839267	-5534.94037	-5534.101098		
Pd-N-1	0.843101	-7043.36166	-7042.518561	-0.039774	-24.96
Pd-Se	0.838005	-7043.33543	-7042.497428	-0.018641	-11.70
Pd-Se-N	0.851179	-6583.11636	-6582.265179	-0.035167	-22.07

4. References

[1] Frisch, M. J.; Trucks, G. W.; Schlegel, H. B.; Scuseria, G. E.; Robb, M. A.; Cheeseman, J. R.;

Scalmani, G.; Barone, V.; Petersson, G. A.; Nakatsuji, H.; Li, X.; Caricato, M.; Marenich, A. V.; Bloino, J.; Janesko, B. G.; Gomperts, R.; Mennucci, B.; Hratchian, H. P.; Ortiz, J. V.; Izmaylov, A. F.; Sonnenberg, J. L.; Williams; Ding, F.; Lipparini, F.; Egidi, F.; Goings, J.; Peng, B.; Petrone, A.; Henderson, T.; Ranasinghe, D.; Zakrzewski, V. G.; Gao, J.; Rega, N.; Zheng, G.; Liang, W.; Hada, M.; Ehara, M.; Toyota, K.; Fukuda, R.; Hasegawa, J.; Ishida, M.; Nakajima, T.; Honda, Y.; Kitao, O.; Nakai, H.; Vreven, T.; Throssell, K.; Montgomery Jr., J. A.; Peralta, J. E.; Ogliaro, F.; Bearpark, M. J.; Heyd, J. J.; Brothers, E. N.; Kudin, K. N.; Staroverov, V. N.; Keith, T. A.; Kobayashi, R.; Normand, J.; Raghavachari, K.; Rendell, A. P.; Burant, J. C.; Iyengar, S. S.; Tomasi, J.; Cossi, M.; Millam, J. M.; Klene, M.; Adamo, C.; Cammi, R.; Ochterski, J. W.; Martin, R. L.; Morokuma, K.; Farkas, O.; Foresman, J. B.; Fox, D. J. Gaussian 16 Rev. C.01, Wallingford, CT, 2016.

[2] Y. Zhao, D.G. Truhlar, The M06 suite of density functionals for main group thermochemistry, thermochemical kinetics, noncovalent interactions, excited states, and transition elements: two new functionals and systematic testing of four M06-class functionals and 12 other functionals, Theoretical Chemistry Accounts. 120 (2007) 215-241. https://doi.org/10.1007/s00214-007-0310-x.

[3] A. Schäfer, C. Huber, R. Ahlrichs, Fully optimized contracted Gaussian basis sets of triple zeta valence quality for atoms Li to Kr, The Journal of Chemical Physics. 100 (1994) 5829-5835. https://doi.org/10.1063/1.467146.

[4] C. Zhan, D.A. Dixon, Absolute Hydration Free Energy of the Proton from First-Principles Electronic Structure Calculations, The Journal of Physical Chemistry A. 105 (2001) 11534-11540. https://doi.org/10.1021/jp012536s.

[5] S.V. Balina, V.V. Russkikh, N.A. Orlova, L.N. Ogneva, V.V. Shelkovnikov, Synthesis of bis(4-hydroxyphenyl) selenide and epoxide and acrylate monomers on this basis, Russian Journal of Organic Chemistry. 51 (2015) 198-201. https://doi.org/10.1134/s1070428015020104.

[6] W. Wang, H. Li, Y. Zhou, J. Pan, Investigation of the mechanism of establishing a solid-water-oil system by metastable droplets and their application in the fabrication of polyol nanosheets for rapid boron removal, Chemical Engineering Journal. 475 (2023) 145930. https://doi.org/10.1016/j.cej.2023.145930.

[7] T. Li, M. Cao, J. Liang, X. Xie, G. Du, Mechanism of Base-Catalyzed Resorcinol-Formaldehyde and Phenol-Resorcinol-Formaldehyde Condensation Reactions: A Theoretical Study, Polymers. 9 (2017) 426. https://doi.org/10.3390/polym9090426.

[8] C. Wang, K. Yang, Q. Xie, J. Pan, Z. Jiang, H. Yang, Y. Zhang, Y. Wu, J. Han, Tandem Efficient Bromine Removal and Silver Recovery by Resorcinol-Formaldehyde Resin Nanoparticles, Nano Letters. 23 (2023) 2239-2246. https://doi.org/10.1021/acs.nanolett.2c04877.

[9] J. Tang, Y. Chen, S. Wang, D. Kong, L. Zhang, Highly efficient metal-organic frameworks adsorbent for Pd(II) and Au(III) recovery from solutions: Experiment and mechanism, Environmental Research. 210 (2022) 112870. https://doi.org/10.1016/j.envres.2022.112870.

[10] F. Wu, H. Li, Y. Pan, Y. Sun, J. Pan, Bioinspired construction of magnetic nano stirring rods with radially aligned dual mesopores and intrinsic rapid adsorption of palladium, Journal of Hazardous Materials. 441 (2022) 129917. https://doi.org/10.1016/j.jhazmat.2022.129917.

[11] F. Wu, H. Li, Y. Pan, Y. Wang, Y. Sun, J. Pan, Sustainable utilization of palladium from industrial catalytic waste by a smart magnetic nano stirring robot, Separation and Purification Technology. 315 (2023) 123536. https://doi.org/10.1016/j.seppur.2023.123536.

[12] F. Wu, A. Haleem, M. Ullah, L. Chen, H. Li, J. Pan, Fabrication of superporous cryogels with amidoxime chelation sites and customizable 3D printing for targeted palladium recovery from secondary resources, Journal of Hazardous Materials. 481 (2024) 136532. https://doi.org/10.1016/j.jhazmat.2024.136532.

[13] S. Akioka, S. Hirai, T. Ise, N. Gando, M.A.H. Alharbi, Selective recovery of palladium by wool resin and woven wool fabric resinrbents, Hydrometallurgy. 203 (2021) 105629. https://doi.org/10.1016/j.hydromet.2021.105629.

[14] H. Dong, S. Ning, Z. Li, S. Xu, S. Zhang, X. Wang, Y. Wang, L. Chen, X. Yin, T. Fujita, M.F. Hamza, Y. Wei, Efficient separation of palladium from high-level liquid waste with novel adsorbents prepared by sulfhydryl organic ligands containing imidazole, thiazole and oxazole composited with XAD7HP, Journal of Water Process Engineering. 53 (2023) 103681. https://doi.org/10.1016/j.jwpe.2023.103681.

[15] Q. Yi, R. Fan, F. Xie, Q. Zhang, Z. Luo, Recovery of Palladium(II) from nitric acid medium using a natural resin prepared from persimmon dropped fruits residues, Journal of the Taiwan Institute of Chemical Engineers. 61 (2016) 299-305. https://doi.org/10.1016/j.jtice.2016.01.009.

[16] M. Can, Emrah Bulut, Mahmut Özacar, Reduction of palladium onto pyrogallol-derived nano-resin and its mechanism, Chemical Engineering Journal. 275 (2015) 322-330. https://doi.org/10.1016/j.cej.2015.04.041.

[17] L. Chen, K. Wu, M. Zhang, N. Liu, C. Li, J. Qin, Q. Zhao, Z. Ye, Synthesis of carbon disulfide modified chitosan resin and its adsorption properties for palladium(II) in wastewater, Chemical Engineering Journal. 466 (2023) 143082. https://doi.org/10.1016/j.cej.2023.143082.

[18] L. Peng, M. Zhang, Z. Dong, W. Qi, M. Zhai, L. Zhao, Efficient and selective adsorption of Pd(II) by amino acid-functionalized cellulose microspheres and their applications in palladium recovery from PCBs leaching solution, Separation and Purification Technology. 301 (2022) 122037. https://doi.org/10.1016/j.seppur.2022.122037.

[19] A.N. Turanov, V.K. Karandashev, O.I. Artyushin, E.V. Sharova, G.K. Genkina, Adsorption of palladium(II) from hydrochloric acid solutions using polymeric resins impregnated with novel N-substituted 2-(diphenylthiophosphoryl)acetamides, Separation and Purification Technology. 187 (2017) 355-364. https://doi.org/10.1016/j.seppur.2017.06.068.

[20] H. Dong, S. Ning, Z. Li, S. Xu, F. Hu, F. Gao, Y. Wang, L. Chen, X.-B. Yin, T. Fujita, M.F. Hamza, Y. Wei, Precise separation and efficient recovery of Pd(II) from high-level liquid waste by XAD-based adsorbents, Rare Metals. 43 (2024) 5372-5390. https://doi.org/10.1007/s12598-024-02711-y.